

Next Generation Very Large Array Memo No. 38

**Subarray Processing for Projection-Based RFI Mitigation in
Radio Astronomical Interferometers**

Mitchell C. Burnett, Brian D. Jeffs, Richard A. Black, and Karl F. Warnick

March 12, 2018

SUBARRAY PROCESSING FOR PROJECTION-BASED RFI MITIGATION IN RADIO ASTRONOMICAL INTERFEROMETERS

MITCHELL C. BURNETT,¹ BRIAN D. JEFFS,¹ RICHARD A. BLACK,¹ AND KARL F. WARNICK¹

¹*Department of Electrical And Computer Engineering, Brigham Young University, Provo, UT 84602, USA*

ABSTRACT

Note: This memo derives from a paper of the same title and authors appearing in the *Astronomical Journal*, volume 155, issue 4, April 2018, © 2018 American Astronomical Society. It is included by permission in the NRAO ngVLA Memo Series.

Radio Frequency Interference (RFI) is a major problem for observations in Radio Astronomy (RA). Adaptive spatial filtering techniques such as subspace projection are promising candidates for RFI mitigation, but for radio interferometric imaging arrays these have primarily been used in engineering demonstration experiments rather than mainstream scientific observations. This paper considers one reason that adoption of such algorithms is limited: RFI decorrelates across the interferometric array because of long baseline lengths. This occurs when the relative RFI time delay along a baseline is large compared to the frequency channel inverse bandwidth used in the processing chain. Maximum achievable excision of the RFI is limited by covariance matrix estimation error when identifying interference subspace parameters, and decorrelation of the RFI introduces error which corrupts the subspace estimate, rendering subspace projection ineffective over the entire array. In this work, we present an algorithm which overcomes this challenge of decorrelation by applying subspace projection via subarray processing (SP-SAP). Each subarray is designed to have a set of elements with high mutual correlation in the interferer for better estimation of subspace parameters. In an RFI simulation scenario for a proposed ngVLA array configuration with 15 kHz channel bandwidth for correlator processing, we show that compared to the former approach of applying subspace projection on the full array, SP-SAP improves mitigation of the RFI on the order of 9 dB. An example of improved image synthesis and reduced RFI artifacts for a simulated image “phantom” using the SP-SAP algorithm is presented.

Keywords: instrumentation: interferometers — methods: statistical — Radio Frequency Interference — RFI Mitigation — methods: Subarray Processing — methods: Subspace Projection

1. INTRODUCTION

In 2015 the National Radio Astronomy Observatory (NRAO) announced that they would begin supporting an effort for the initial concept, design, and development of a large area radio instrument optimized for imaging thermal emissions down to milliarcsecond scales. The current Very Large Array (VLA) site in New Mexico is a possible location for the new interferometer and is known as the Next Generation Very Large Array (ngVLA). A proposed array design uses 300 telescopes operating from 1 GHz to 115 GHz configured with a dense core and longest distance between an antenna pair (baseline) spanning 300 km (Carilli 2015, 2016). The Square Kilometre Array (SKA) (Davidson 2012) is another, even more mature, example of a major new radio interferometer project which plans significant leaps in numbers of antenna, increased baseline lengths, and wider operating bandwidths, all with the aim of achieving improved resolution and sensitivity over their predecessors.

This paper presents a new algorithm to improve performance of array processing spatial filtering methods which cancel radio frequency interference (RFI) in large interferometric synthesis imaging arrays. The algorithm is suitable for many existing arrays, (e.g., VLA, MEERKAT, ASKAP, WSRT) but will be particularly beneficial with the extremely long baselines of the ngVLA and SKA.

Even when such arrays are sited in radio quiet zones, RFI will pose a major threat to some of the science goals for these and other instruments. Satellite radio downlinks are problematic all over the world, and observatories and institutes are reporting damaging levels of RFI to the extent that data corruption occurs in up to 100% of their observations for a given frequency band (Hoppmann et al. 2015; Otto et al. 2016; Sokolowski et al. 2015; Offringa, A. R. et al. 2012). For example, important frequency bands for observing moderately red-shifted HI (neutral hydrogen) emissions are now almost entirely blocked by strong RFI due to downlinks from the GPS, GLONASS, Galileo, and COMPASS navigation satellites, and IRIDIUM communication satellites (Ellingson et al. 2001, 2000; Vine et al. 2016; Indermuehle et al. 2016).

Adaptive linear-subspace-projection-based spatial filtering involves estimating interfering array spatial signatures (gain and phase responses toward the RFI) and then using this information to form deep cancellation nulls on the interferer by applying a projection into the sensor vector subspace orthogonal to the interferer. This provides the capability to *observe through* strong RFI conditions rather than just discarding corrupted data by flagging or blanking, or merely avoiding it by observing in other frequency channels (Anonymous 2013).

Subspace projection techniques for interferometric arrays were first proposed in Leshem et al. (2000); Leshem & van der Veen (2000). While spatial filtering methods are promising in simulation, adoption by astronomers in active science

observations has been very slow. This is partially due to some poor canceling performance in several practical observation scenarios. For example, *i*) when the interference-to-noise power ratio (INR) is low, or *ii*) when RFI motion is fast relative to the maximum array aperture dimension and the correlator integration dump interval, or *iii*) when correlation of the RFI is weak because of long baselines coupled with insufficiently narrow correlator processing channel bandwidths (Black et al. 2015; Black 2017).

In these situations, accurate estimation of interference subspace parameters is difficult, and conventional adaptive cancelers perform poorly. However, some effective solutions have been proposed. RFI motion can be overcome with subspace models and tracking techniques as in Landon et al. (2012); Black (2017); Ellingson & Hampson (2002); Hellbourg (2015). Use of auxiliary antennas that track and measure RFI to provide a high INR copy of the undesired signal has been shown to improve mitigation (Jefferies et al. 2003, 2005). But to date, no method has been proposed to address decorrelation of the RFI.

In this work, we address the problem of decorrelation and present an algorithm for applying subspace projection on subsets of array elements (or subarrays) where there is guaranteed high RFI mutual correlation. This enables better subspace parameter estimates and subsequently improves RFI excision.

The paper is organized as follows. Section 2 presents our signal model for imaging array systems. In Section 3 we supplement and extend the analysis given in Thompson (1982) to show the effects of interference decorrelation across large interferometric baselines. In Section 4 we review prior subspace projection work and show how RFI decorrelation corrupts interference subspace estimates. Section 5 presents the new algorithm for implementing subspace projection via subarray processing (SP-SAP) on large interferometry arrays to overcome RFI decorrelation. Results for simulation scenarios are given in Section 6 to demonstrate performance. We conclude in Section 7 with a discussion about future work and applications to current array systems.

2. SIGNAL MODEL AND SYNTHESIS IMAGING EQUATIONS

This section defines only the relevant geometry, notation and signal models needed to provide a foundation for our discussion on spatial filtering, and to develop the proposed algorithm. For additional detail on the theory and practice of radio synthesis imaging we refer the reader to Thompson et al. (2001) and Taylor et al. (1999). A tutorial reference using the same notation as in the following development is found in Swindlehurst et al. (2013). Figure 1 depicts a simple imaging scenario for an interferometry array system as explained in the following discussion.

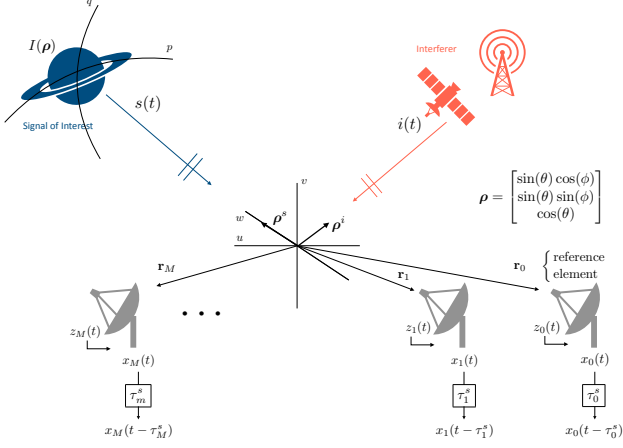


Figure 1. Simple imaging scenario for a synthesis imaging array. Given azimuth and elevation angles direction cosines can be used to calculate a propagation vector ρ for a signal of interest (SOI) and interferer(s). The array has been co-phased with inserted time delays to image a celestial SOI. Interferers corrupt the visibilities for the SOI and introduce artifacts in the resulting radio image.

Consider imaging a celestial signal of interest (SOI) with an M -element radio interferometric array. The position of a particular array element is specified in the (u, v, w) rectilinear coordinate system in units of wavelength (λ) at a narrowband source observation frequency f_c . Broadband SOIs are observed using many such narrowband channels. Vector $\mathbf{r}_m = (u_m, v_m, w_m)$ describes the position of the m th element relative to an arbitrary coordinate axis origin. The SOI observation is projected onto the celestial sphere, on which the imaging coordinate axis (p, q) is defined to be aligned with and parallel to the (u, v) axes from the (u, v, w) coordinate system at the array. A radio image is formed by estimating the intensity distribution $I(\rho)$ of the electric field arriving from the direction described by unit-length propagation vectors $\rho = (u_\rho, v_\rho, w_\rho)$ for each pixel within the imaging field of view. A different $\rho_{p,q}$ vector points to each distinct pixel, (p, q) . Since $\rho_{p,q}$ is unit length and (p, q) is aligned and parallel to (u, v) , $\rho_{p,q}$ may also be expressed in terms of (p, q) ; $\rho_{p,q} = (p, q, \sqrt{1-p^2-q^2})$. Wavefronts from each pixel in the celestial SOI are perpendicular to the propagation vector, and travel along the vector.

For notational convenience, we drop the subscript notation on $\rho_{p,q}$ denote ρ^s to represent the vector that points to the origin in the imaging coordinate plane. Thus $\rho^s = (0, 0, 1)$. This is the source reference position, and has at times been referred to as the *phase center* of the image. Also, the array element most distant from the SOI is arbitrarily designated as a reference element and is indexed as $m = 0$. Relative to this reference element, the time difference of arrival for the SOI wavefront at the m th element is denoted as τ_m^s . This

geometric delay term is a function of the distance between the two elements, and may be expressed as

$$\tau_m^s = \frac{(\mathbf{r}_m - \mathbf{r}_0)^T \rho^s}{c}, \quad (1)$$

where c is the speed of light. For the reference element, $\tau_0 = 0$. In the interferometric image synthesis processing chain, time delays are first applied to receiver outputs to compensate for this geometric delay and co-phase the array to the phase center of the image.

Let the passband receiver output for the m th array element (antenna) be represented by its complex-valued baseband equivalent signal $x_m(t)$, (i.e., the narrowband channel is mixed down to d.c. with an image rejection mixer to produce a representation using in-phase, real, and quadrature, imaginary, components). Gather these $x_m(t)$ from all array elements to form the signal vector $\mathbf{x}(t)$. The system output vector time signal is modeled as a narrowband channel and is the linear combination of signal, interference, and noise given by

$$\begin{aligned} \mathbf{x}(t) &= [x_1(t), x_2(t), \dots, x_M(t)]^T \\ &= \mathbf{a}(\theta_s)s(t) + \mathbf{a}(\theta_i)i(t) + \mathbf{z}(t). \end{aligned} \quad (2)$$

The vectors $\mathbf{a}(\theta_s)$ and $\mathbf{a}(\theta_i)$ represent the previously mentioned array spatial signatures (A.K.A. steering vector) in the direction of the SOI and interferer respectively. For an extended SOI, we consider θ_s to be the direction to a single pixel in the image for the SOI. All θ values are two dimensional spherical angles. The m th entry in $\mathbf{a}(\theta)$ is the narrowband complex magnitude and phase response of the array to a unit amplitude signal arriving from direction angle θ . Signals $s(t)$, $i(t)$, and $\mathbf{z}(t)$ are modeled as zero-mean proper Gaussian complex-valued random processes and represent the SOI, man-made interfering signal, and noise respectively. The term ‘‘proper’’ denotes that the real and imaginary parts of a random process are mutually uncorrelated.

For the limited field of view in this imaging scenario, the fundamental quantity used to estimate the intensity image of the electric field distribution, $I(\rho)$, from receiver outputs is known as the visibility function (Thompson et al. 2001). In the absence of noise and interference the visibility function is approximately given by

$$\begin{aligned} V(\mathbf{r}_l, \mathbf{r}_m) &= E [x_l(t)x_m^*(t)] \\ &= \int \int |A(\rho)|^2 I(\rho) e^{-j2\pi(\rho - \rho^s)^T (\mathbf{r}_l - \mathbf{r}_m)} d\rho, \end{aligned} \quad (3)$$

where $E[\cdot]$ is the expectation operator and $*$ denotes complex conjugate. The function $A(\rho)$ represents the antenna response pattern for each array element, and is assumed to be identical across elements. The difference vector $\mathbf{r}_l - \mathbf{r}_m$ is referred to as a baseline between elements l and m . Expressing

these baselines in (u, v) coordinates and assuming a continuous range of all possible baseline vectors are available leads to the visibility function form:

$$V(u, v) = \int \int |A(p, q)|^2 I(p, q) e^{-j2\pi(up+vq)} dp dq. \quad (4)$$

An intuitive interpretation of (4) is that the imaging information is related to the spatial cross-correlation of antenna pairs (baselines) through a Fourier transform relationship.

However, since the available baselines are limited to the discrete set of antenna pairs (l, m) , we observe only an irregularly sampled version, $V(u_{l,m}, v_{l,m})$, of the visibility function of (4). These pairs may be collected into a single matrix

$$\mathbf{R} = E [\mathbf{x}(t)\mathbf{x}^H(t)] = \begin{bmatrix} V(\mathbf{r}_0, \mathbf{r}_0) & \dots & V(\mathbf{r}_0, \mathbf{r}_{M-1}) \\ \vdots & \ddots & \vdots \\ V(\mathbf{r}_{M-1}, \mathbf{r}_0) & \dots & V(\mathbf{r}_{M-1}, \mathbf{r}_{M-1}) \end{bmatrix}, \quad (5)$$

where H is matrix conjugate transpose. This matrix is recognized as the array autocorrelation matrix (or covariance matrix since $\mathbf{x}(t)$ is zero mean) and the entries are known as visibilities. In general, RFI and noise are present and are statistically independent from each other and the SOI. Therefore, the visibility matrix can be expressed as

$$\begin{aligned} \mathbf{R} &= E [\mathbf{x}(t)\mathbf{x}^H(t)] \\ &= \mathbf{R}_s + \mathbf{R}_i + \mathbf{R}_z, \end{aligned} \quad (6)$$

where \mathbf{R}_s , \mathbf{R}_i , and \mathbf{R}_z are the individual covariance matrices for SOI, interferer, and noise respectively. The true covariances are not known, therefore \mathbf{R}_s can only be observed through a sample estimate, $\hat{\mathbf{R}}$ (where $\hat{}$ indicates an estimated quantity), which includes the undesired contributions from \mathbf{R}_i and \mathbf{R}_z , and sample estimation error \mathbf{E} .

Most RFI cancelling array-based spatial filtering algorithms use the sample spatial covariance matrix $\hat{\mathbf{R}}$ to estimate the array response of the interferer in order to subsequently remove interference (Anonymous 2013) (Sec. 5), (Leshem et al. 2000; Fridman & Baan 2001; Ellingson & Hampson 2002; Jeffs et al. 2005, 2008; Hellbourg et al. 2012; Hellbourg 2015; Ford & Buch 2014; van der Veen et al. 2005; Black et al. 2015).

These estimates are computed by the correlator of a digital back end processing system for a range of narrowband channels across the full processing bandwidth. For a single frequency channel, the output of the correlator is given by

$$\begin{aligned} \hat{\mathbf{R}}_j &= \frac{1}{N} \sum_{n=jN}^{(j+1)N-1} \mathbf{x}[n]\mathbf{x}^H[n], \quad 0 \leq j \leq J-1 \\ &= \mathbf{R}_s + \mathbf{R}_{i,j} + \mathbf{R}_z + \mathbf{E}_j, \end{aligned} \quad (7)$$

where due to RFI motion the sample covariances must be re-computed frequently using a relatively small number, N , of samples over J periods, on ms time-scales. These are called short-term integrations (STIs). Over the period of one STI the spatial signature of the interferer is assumed to be stationary. The STIs are combined over a long-term integration (LTI) period of JN samples, on the order of 10 s, as the overall LTI estimate $\hat{\mathbf{R}}$ used for image synthesis. The estimates of \mathbf{R}_s and \mathbf{R}_z are also assumed to be stationary over both long and short-term integrations.

In practice, imaging arrays take advantage of the Earth's rotation by recomputing the visibility matrix on medium time-scales. Each new computed set of visibilities has a unique rotated set of baselines, further filling in the (u, v) sample space in (4). An RFI cancelling projection operator would be computed and applied separately for each new set of baseline orientations.

3. RFI DECORRELATION

Long baseline arrays like the ngVLA and SKA are problematic for projection-based RFI cancellation. Indeed any adaptive cancelling algorithm based on covariance estimates (multiple sidelobe canceler, MMSE array filter, etc.) would suffer similar limitations. This is because the RFI, even if visible in all elements, is decorrelated over the longer baselines. This makes it difficult to estimate RFI spatial parameters needed for effective projection cancellation.

Figure 2 presents the proposed ngVLA configuration of 300 elements with longest baselines of 300 km we will use throughout this work to illustrate the effects of RFI decorrelation on projection cancellation. Also shown is a magnification of the core at 15 km, 5 km, and 3 km radius views.

Large synthesis arrays such as the ngVLA are less sensitive to interference than single-dish telescopes (Thompson 1982). In his analysis, Thompson presented threshold levels for which RFI is detrimental to observations on the VLA, as well as how similar levels could be computed to extend to other arrays. While it is true that threshold levels are higher due to RFI decorrelation in these long baseline arrays, interference is still clearly present in resulting maps and images.

There are two effects that Thompson investigated which reduce the response of the array to an interferer. The first is the averaging effect. The argument is that relative to the earth, a ground-based interferer is stationary, and as the array tracks the SOI there is a slight change in relative phase. This relative phase difference is known as the fringe frequency (Taylor et al. 1999). At the time of image formation, due to the significantly large number of (u, v) samples that are interpolated onto a rectangular grid for an FFT-based Fourier inversion of (4), the averaging of these relative phase differences at individual points over the entire grid reduces interferer signal

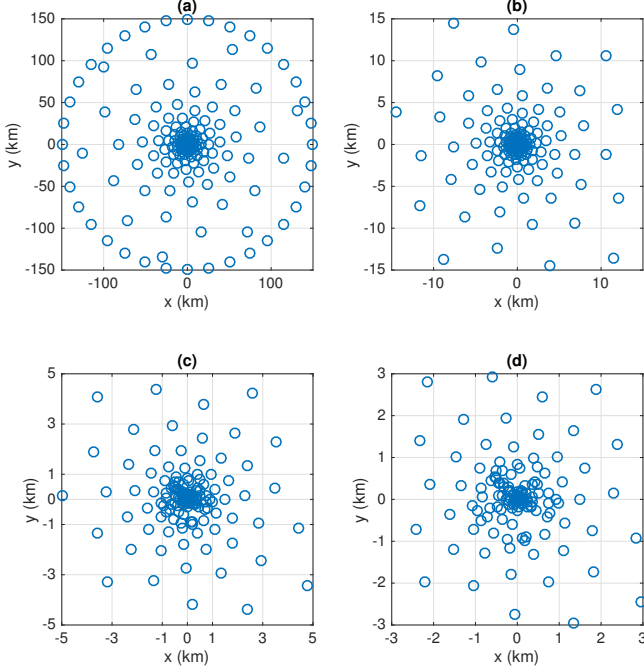


Figure 2. (a) One proposed ngVLA configuration consists of 300 antennas with the longest baselines extending to 300 km. This configuration also includes a dense core with 20% of the elements inside the radius of 0.6 km. (b)-(d) Magnified into the core at 15 km, 5 km and 3 km radius scales respectively.

levels due to destructive cancelling of the RFI terms being summed out of phase.

The second effect is a result of the phase propagation that occurs due to the geometric delay of the interferer across the array. The geometric delay for the interferer is similar to the definition of (1) but is now dependent on the propagation vector ρ^i . Let this delay be specified as τ_m^i . Before applying the co-phasing time delays which compensate for the geometric delay due to the SOI, the output of the m th element in response to a wave originating from a point source at the phase reference location ($p = 0, q = 0$) in the presence of single interfering source is

$$x_m(t) = a_m(\theta_s)s(t + \tau_m^s) + a_m(\theta_i)i(t + \tau_m^i) + z_m(t). \quad (8)$$

Subsequently, applying the co-phasing time delay yields,

$$x_m(t - \tau_m^s) = a_m(\theta_s)s(t) + a_m(\theta_i)i(t + \tau_m^i - \tau_m^s) + z_m'(t). \quad (9)$$

Because the noise process $z_m(t)$ is an independent and identically distributed wide sense stationary process, the co-phasing delay does not affect the statistics of the process and we can consider it as if no delay had been added to the noise. We see that for the phase reference location in the imaging plane, the output at time t across the entire array will not depend on the propagation path of the SOI. Or, in other words,

when the correlator produces the visibility matrix it will compare the signal between elements as if it had coherently sampled the entire time aligned wavefront for the SOI.

However, the same cannot be said of the interfering source. The time series for the interferer is affected by the geometric delay as it propagates across the array, as well as the co-phasing time delay resulting in an effective bulk geometric delay of $\tau_m^b = \tau_m^i - \tau_m^s$. For a given processing bandwidth β , this bulk geometric delay results in phase propagation across the array given by

$$\begin{aligned} \psi_m &= 2\pi(\tau_m^i - \tau_m^s)\beta \\ &= 2\pi\tau_m^b\beta. \end{aligned} \quad (10)$$

This phase propagation results in incoherence of the interferer at the correlator and is characterized by the correlation function

$$\gamma(\tau_m^b; \beta) = \frac{\sin(\pi\tau_m^b\beta)}{\pi\tau_m^b\beta} = \text{sinc}(\tau_m^b\beta), \quad (11)$$

where the sinc function is defined as

$$\text{sinc}(x) = \frac{\sin(\pi x)}{\pi x}.$$

Note that we can manipulate (10) to express (11) in terms of the phase propagation

$$\gamma(\psi_m) = \text{sinc}\left(\frac{\psi_m}{2\pi}\right). \quad (12)$$

These correlation functions manifest a fundamental trade-off between baseline length, processing bandwidth, and the effects on correlation of the RFI in the visibilities. For narrow processing bandwidths on the order of a few Hz to a few kHz, which would be used for example in the processing of narrowband galactic emissions, the correlations vary slowly and significant decorrelation would only begin to occur at a few hundred kilometers. As the processing bandwidth increases for the observation of more continuum sources, the correlations decay more rapidly as the effective projected baseline length for the bulk geometry delay increases. Figure 3 depicts the decorrelation of an interferer for an antenna pair on the ngVLA for various processing bandwidths and baseline lengths. The interferer is arriving endfire to the baseline vector for a maximum, worst case, effective projected baseline length.

We can see that in general, correlations do decay, however, only in the limit are they zero. For most practical processing bandwidths there will be significant correlations at several elements because of compact core configurations. This suggests that RFI may pose a threat to some observations and that RFI mitigation techniques can be used to ease that burden.

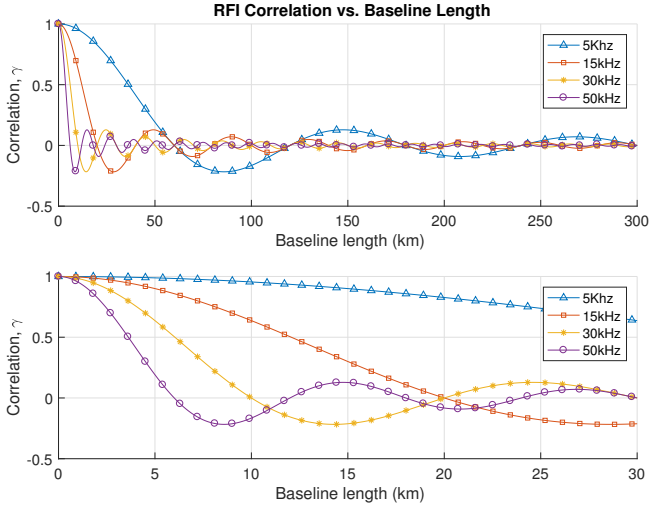


Figure 3. Extent of RFI decorrelation for an antenna pair at different processing bandwidths. The signal is arriving endfire for a maximum projected baseline length. In general, the correlation varies slowly for narrowband channel processing. As the bandwidth increases the correlations decreases more rapidly. With a dense core on the ngVLA, there will be significant correlation potentially corrupting images without mitigation.

In theory, equation (11) suggests that one could always operate on sufficiently narrow channel bandwidths to support subspace projection (see Section 4) involving arbitrarily long baselines with negligible RFI decorrelation. However, practical real-time correlator implementation constraints make this impossible. For example, halving the processor channel bandwidth at the correlator doubles the data rate for transport and storage of correlator visibility outputs. Twice as many visibility matrices (of the same size as the original) are produced. For long baseline arrays, when imaging over a fixed total bandwidth, a limit is soon reached where the instrument computing hardware/software/storage units cannot support the data rate needed to maintain RFI correlation across a sufficient number of baselines to yield effective subspace projection RFI canceling. The algorithm presented in Section 5 eases these constraints.

4. SUBSPACE PROJECTION

In the presence of Q interferers, subspace projection is a null-forming algorithm that cancels interferers by applying projection operator \mathbf{P}_j to the $M \times M$ estimated sample covariance matrix $\hat{\mathbf{R}}_j$ for a given STI interval. In the analysis that follows we drop the subscript j , and it is implied that the calculation of a projection matrix is done for each STI. The projection is designed to be approximately orthogonal to the subspace that spans the spatial signature of the Q interferers. To design the projection matrix a dominant eigenvector analysis is performed on the sample covariances. The eigenvector

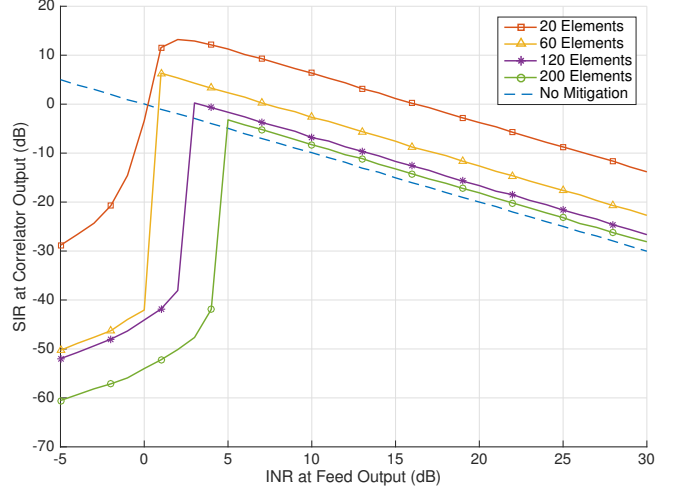


Figure 4. Illustration of the effectiveness of subspace projection on the ngVLA at a center frequency of 2.6 GHz and a processing bandwidth of 20 kHz. Increasing the number of elements included in the subspace estimation process also increases the number of elements at longer effective projected baseline. With a large number of elements at longer baselines subspace projection becomes less effective at providing cancellation to the RFI.

decomposition of the sample covariance matrix is

$$\hat{\mathbf{R}} = \mathbf{U}\mathbf{\Lambda}\mathbf{U}^H, \quad (13)$$

where the columns of \mathbf{U} are the eigenvectors of $\hat{\mathbf{R}}$ and the diagonal entries of $\mathbf{\Lambda}$ are the corresponding eigenvalues. Assuming the interferers are much stronger than the SOI and system noise, the resulting eigenvector matrix \mathbf{U} can be sorted and partitioned as $\mathbf{U} = [\mathbf{U}_i | \mathbf{U}_{s+z}]$, where \mathbf{U}_i represents the eigenvectors corresponding to the Q largest eigenvalues. The conventional subspace projection matrix \mathbf{P}_{SP} is then formed as

$$\mathbf{P}_{\text{SP}} = \mathbf{I} - \mathbf{U}_i(\mathbf{U}_i^H \mathbf{U}_i)^{-1} \mathbf{U}_i^H. \quad (14)$$

The projection is applied to $\hat{\mathbf{R}}$ by left and right multiplication,

$$\tilde{\mathbf{R}} = \mathbf{P}_{\text{SP}} \hat{\mathbf{R}} \mathbf{P}_{\text{SP}}^H, \quad (15)$$

resulting in the filtered visibility matrix $\tilde{\mathbf{R}}$, where the Q interferers have been largely eliminated. Using the estimated subspace, the projections will only be approximately orthogonal to the RFI and therefore introduce a slight bias in \mathbf{R}_s . This can be corrected on average as show in [Leshem & van der Veen \(2000\)](#); [Jeffs et al. \(2005\)](#); [Raza et al. \(2002\)](#).

A metric used to measure performance of a mitigation algorithm is the signal-to-interference power ratio (SIR) at the filter output given by

$$\text{SIR} = \frac{\text{Tr}\{\mathbf{P}\mathbf{R}_s\mathbf{P}^H\}}{\text{Tr}\{\mathbf{P}\mathbf{R}_i\mathbf{P}^H\}}, \quad (16)$$

where $\text{Tr}\{\cdot\}$ is the matrix trace operation. This metric compares the performance of the level to which \mathbf{P} attenuates the interference relative to attenuation in the signal.

Figure 4 illustrates how SIR is affected by baseline length for the ngVLA configuration. The abscissa of this plot is the INR at the element antenna terminals. This detailed simulation computes the visibility matrix and applies subspace projection across M elements starting from the central core and extending outward. Included is a curve labeled “no-mitigation,” which is the resulting SIR had no projection been applied. Shown by (12), the level of correlation for the interferer is well-defined in terms of the phase propagation due to the processing bandwidth and bulk geometric time delay. Small M yields a dense set of elements in the central core over baselines where the geometric delay results in a significant measure of coherence in the interferer. Figure 4 shows that the greatest attenuation to the interferer relative to the SOI is achieved for a compact array with small M , and that the effectiveness of subspace projection decreases with larger M across baselines where larger geometric time delays results in less correlation between array elements.

There are two factors which contribute to the decreased effectiveness of subspace projection across large baselines as seen in Figure 4. The first factor is that the underlying assumption of RFI subspace estimation has been violated by using weak coherence levels in the sample estimate. The design of \mathbf{P}_{SP} had assumed interference is the strongest component present in the sample covariances. On the far baselines the dominant component in the covariance is now the SOI or noise, preventing accurate estimation of the interferer subspace. This issue would arise even if an exact \mathbf{R} was available with no estimation error, and is related to the partitioning step to select \mathbf{U}_i from \mathbf{U} . The second factor is that the level of sample estimation error due to \mathbf{E} in (7) has contributions from not only \mathbf{R}_i but \mathbf{R}_s and \mathbf{R}_z as well. The contributions to \mathbf{E} are proportional to the scale of the entries in the estimated covariances and inversely proportional to the number of samples N (Kaveh & Barabell 1986; Kot et al. 1995). On long baselines where entries in \mathbf{R}_i are small, these small values can be overwhelmed by the proportionally larger entries in \mathbf{E} due to \mathbf{R}_s and \mathbf{R}_z (Jeffs et al. 2005).

5. SUBSPACE PROJECTION VIA SUBARRAY PROCESSING (SP-SAP)

Due to considerations discussed in section 4, achieving an adequate estimate of the interferer subspace is not possible using the entire array covariance matrix \mathbf{R} directly. In the proposed subarray processing method, modifications are made to the subspace projection algorithm to improve estimates of the RFI spatial signature. This allows spatial filtering to be a viable option on large interferometers in the growing presence of RFI.

The expression in (9) for bulk geometric time delay of the interferer can be expanded using definitions of delays for the SOI and interferer to become

$$\begin{aligned}\tau_m^b &= \tau_m^i - \tau_m^s \\ &= \frac{(\mathbf{r}_m - \mathbf{r}_0)^T \boldsymbol{\rho}^i}{c} - \frac{(\mathbf{r}_m - \mathbf{r}_0)^T \boldsymbol{\rho}^s}{c} \\ &= \frac{(\mathbf{r}_m - \mathbf{r}_0)^T (\boldsymbol{\rho}^i - \boldsymbol{\rho}^s)}{c}.\end{aligned}\quad (17)$$

Substitution into (10) yields the phase change for RFI across the array relative to the reference antenna \mathbf{r}_0 :

$$\psi_m = 2\pi \frac{(\mathbf{r}_m - \mathbf{r}_0)^T (\boldsymbol{\rho}^i - \boldsymbol{\rho}^s)}{c} \beta. \quad (18)$$

The difference between the SOI and interference propagation vectors can be thought of as the effective propagation vector (after inserted time delays to co-phase the array to the SOI) for the interference. Planes perpendicular to this vector represent regions of constant RFI phase across the array.

SP-SAP uses ψ_m as a metric to partition the full M -element array into K subarrays. The k th subarray is denoted as L_k and is the set of elements satisfying

$$L_k = \{m : \zeta_{k-1} \leq \psi_m < \zeta_k\} \quad \forall m, \quad (19)$$

where $\zeta_k = \zeta_{k-1} + \psi_{\text{thresh}}$ with $\zeta_0 = 0$, and ψ_{thresh} is a user defined parameter. Any two elements within a subarray have a phase propagation difference less than ψ_{thresh} . Grouping the elements in this way creates a set of smaller subarrays with elements aligned perpendicular to the effective propagation vector, thus placing elements in the planes of constant phase. Therefore, each subarray is designed to guarantee high mutual RFI correlation among its own elements to better estimate the interference subspace and project out RFI in its local group.

The algorithm for partitioning subarrays is shown in Table 1 and described in the following example. Results showing the positioned subarrays when applied to the ngVLA are shown in Figure 5.

1. Select a phase threshold, ψ_{thresh} .
2. Compute ψ_m using (18) for each element of the full array and sort in ascending order. Zero relative phase is assigned arbitrarily to the reference element $m = 0$.
3. Initialize $k = 1$ and the range of allowed phase in (19) with $\zeta_0 = 0$ and $\zeta_1 = \psi_{\text{thresh}}$.
4. Using (19) for subarray L_1 , compare entries in the sorted array of ψ_m to the range of allowed phase and group elements into L_1 until no other element satisfies the current range condition.

Table 1. Subarray Formation

Algorithm:
Given ψ_{thresh} and the set of M array elements
Compute $\psi_m = 2\pi \frac{(\mathbf{r}_m - \mathbf{r}_0)^T (\boldsymbol{\rho}^i - \boldsymbol{\rho}^s)}{c} \beta$, for $m = 0, 1, \dots, M-1$
Sort the ψ_m values
$k = 1, \zeta_0 = 0$
while array elements remain unassigned to a subarray:
$\zeta_k = \zeta_{k-1} + \psi_{\text{thresh}}$
$L_k = \{m : \zeta_{k-1} \leq \psi_m < \zeta_k\} \quad \forall \quad m$
$k = k + 1$

NOTE—Subarrays are subsets of the entire set of elements. Any two elements within a subarray have a phase propagation difference less than ψ_{thresh} .

5. Increment k and update ζ_k .
6. Continue to use (19) to compare remaining entries of the sorted array of ψ_m and group elements into subarray L_k .
7. Repeat steps 5 and 6 until all elements in the sorted array of ψ_m have been assigned to a subarray.

The projection matrix formed from the resulting subarrays will better project out RFI in the local grouped elements. To apply subspace projection to the visibility matrix, \mathbf{P}_k is computed for each subarray and combined to form the block diagonal matrix \mathbf{P}_{SAP} ,

$$\mathbf{P}_{\text{SAP}} = \begin{bmatrix} \mathbf{P}_1 & 0 & 0 & 0 \\ 0 & \mathbf{P}_2 & 0 & 0 \\ 0 & 0 & \ddots & 0 \\ 0 & 0 & 0 & \mathbf{P}_K \end{bmatrix}. \quad (20)$$

Any projection matrix must satisfy the condition that it is symmetric and idempotent (i.e. $\mathbf{P}\mathbf{P} = \mathbf{P}$). Note that \mathbf{P}_{SAP} satisfies both of these properties.

In the process of assigning subarrays, the array elements have gone from an arbitrarily indexed set to an ordered set. Elements of vector $\mathbf{x}(t)$ must then be reordered to be compatible with new projection matrix \mathbf{P}_{SAP} . This is quickly achieved using a selection matrix \mathbf{S} . Sparse matrix \mathbf{S} has a single non-zero entry of one in each row and column. For example, if array element n in $\mathbf{x}(t)$ is to be moved to the m th element location in the reordered vector $\mathbf{x}'(t)$, then \mathbf{S} has a one in row m and column n . The transformation is reversed

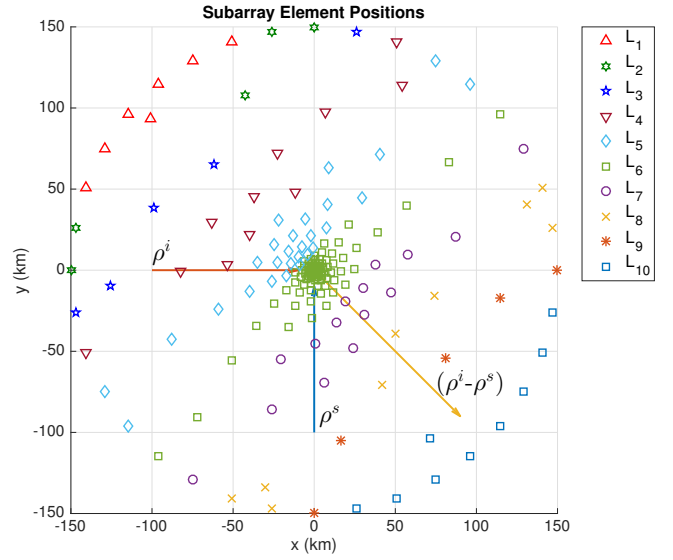


Figure 5. Resulting subarrays after being organized based on the phase propagation metric. This metric orients the subarrays perpendicular to the effective propagation vector $\boldsymbol{\rho}^i - \boldsymbol{\rho}^s$. To form the subarrays shown, the phase threshold was chosen to be high to exaggerate the illustration of the subarrays and their orientation. A small phase threshold will result in more subarrays with less elements per subarray. Conversely, a high threshold results in less subarrays with more elements per subarray.

with left multiplication by \mathbf{S}^T :

$$\begin{aligned} \mathbf{x}'(t) &= \mathbf{S}\mathbf{x}(t) \\ \mathbf{x}(t) &= \mathbf{S}^T \mathbf{x}'(t). \end{aligned} \quad (21)$$

The reordered covariance matrix is computed as

$$\begin{aligned} \mathbf{R}' &= E [\mathbf{x}'(t)\mathbf{x}'^H(t)] \\ &= E [\mathbf{S}\mathbf{x}(t)\mathbf{x}^H(t)\mathbf{S}^T] \\ &= \mathbf{S}\mathbf{R}\mathbf{S}^T, \end{aligned} \quad (22)$$

and projecting out RFI is now straightforward by applying \mathbf{P}_{SAP} to the reordered sample covariance matrix,

$$\tilde{\mathbf{R}}' = \mathbf{P}_{\text{SAP}}\mathbf{S}\mathbf{R}\mathbf{S}^T\mathbf{P}_{\text{SAP}}^H. \quad (23)$$

This matrix is then transformed back to the original order,

$$\tilde{\mathbf{R}} = \mathbf{S}^T\mathbf{P}_{\text{SAP}}\mathbf{S}\mathbf{R}\mathbf{S}^T\mathbf{P}_{\text{SAP}}^H\mathbf{S}, \quad (24)$$

resulting in the final filtered visibility matrix. Defining $\mathbf{P}'_{\text{SAP}} = \mathbf{S}^T\mathbf{P}_{\text{SAP}}\mathbf{S}$, it is easy to see that SP-SAP takes on the familiar form of subspace projection,

$$\tilde{\mathbf{R}} = \mathbf{P}'_{\text{SAP}}\hat{\mathbf{R}}\mathbf{P}'_{\text{SAP}}{}^H. \quad (25)$$

6. SIMULATION RESULTS

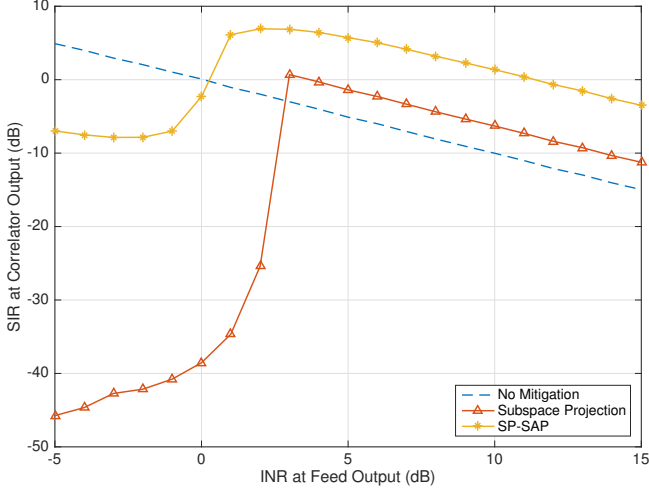


Figure 6. Comparison of SIR post-mitigation at the correlator output. SP-SAP is able to mitigate the RFI at lower INRs and consistently improves the SIR as compared to subspace projection over the entire array.

In this section we compare simulation results for SP-SAP and the conventional approach of applying subspace projection directly over the entire array. In both simulations, the full array for the ngVLA configuration of Figure 2 is used. The SOI is a hypothetical galactic signal at 2800 MHz with a single interferer. Processing bandwidth is 15 kHz to satisfy the narrowband assumption with respect to the interferer. In these simulations we assume short integration periods are used therefore the interferer can be approximated as stationary relative to the array.

Another performance metric for an interference mitigation algorithm is the normalized mean square error in $\tilde{\mathbf{R}}_s$ given by

$$\epsilon_s^2 = \frac{\|\tilde{\mathbf{R}}_s - \mathbf{R}_s\|_F^2}{\|\mathbf{R}_s\|_F^2}, \quad (26)$$

where $\tilde{\mathbf{R}}_s = \mathbf{P}\mathbf{R}_s\mathbf{P}^H$ and $\|\cdot\|_F$ is the Frobenius norm. This metric measures post-mitigation bias introduced by \mathbf{P} in \mathbf{R}_s . Also, we define the attenuation levels for interference and SOI respectively as

$$\alpha_i = \frac{\text{Tr}\{\mathbf{R}_i\}}{\text{Tr}\{\mathbf{P}\mathbf{R}_i\mathbf{P}^H\}},$$

$$\alpha_s = \frac{\text{Tr}\{\mathbf{R}_s\}}{\text{Tr}\{\mathbf{P}\mathbf{R}_s\mathbf{P}^H\}}. \quad (27)$$

Metrics α_i and α_s show the overall effectiveness of removing power from the interferer as well as undesired SOI attenuation.

Figure 6 compares output SIR for subspace projection and SP-SAP across the whole array. Consistent with Figure 4,

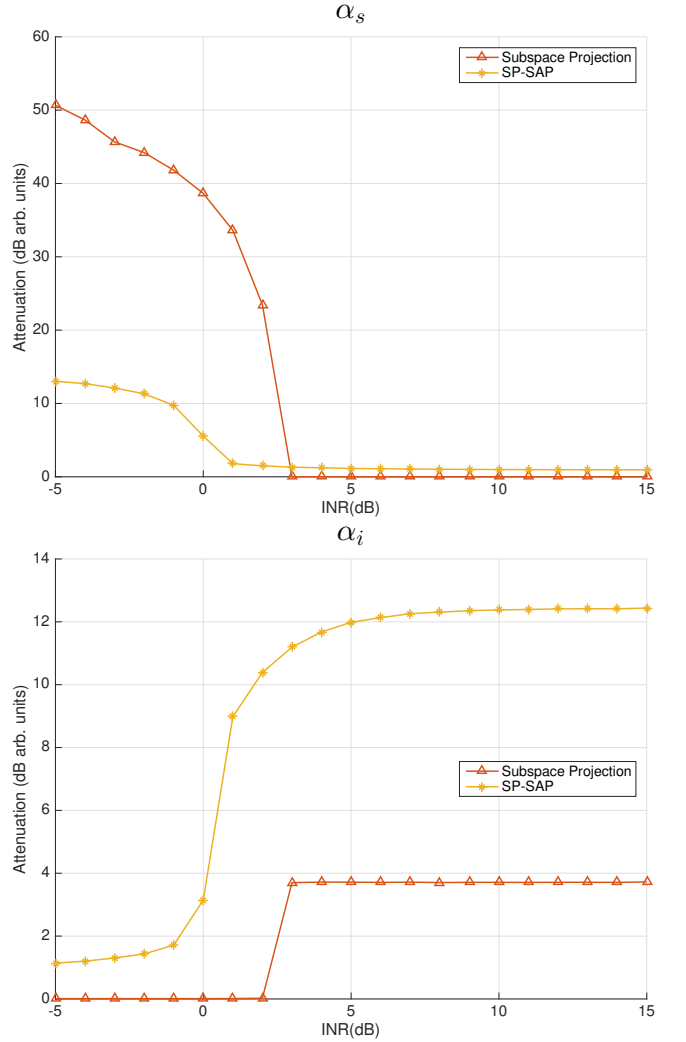


Figure 7. Post-mitigation attenuation to the SOI (top) and RFI (bottom). Subspace projection achieves a modest level of attenuation to the RFI while SP-SAP increases the overall mitigation by 9 dB. SP-SAP does introduce a slight 1 dB of attenuation to the SOI, however, bias corrections can be applied on a per subarray basis to restore the SOI.

due to sample estimation error, subspace projection using the full array does not achieve a satisfactory level of interference cancellation. However, SP-SAP is able to begin cancelling RFI at weaker INR levels and achieves better overall cancellation.

Attenuation factors α_s and α_i are shown in Figure 7. Compared to SP-SAP, subspace projection does better at preventing bias to the SOI. However, examination of the interferer attenuation shows that the 1 dB SOI attenuation results in more than a 9 dB improvement in interference cancellation. No bias correction has been made and so any losses in the SOI could still be recovered while achieving the same level of RFI attenuation (Leshem et al. 2000; Leshem & van der Veen 2000; Jeffs et al. 2005; Raza et al. 2002).

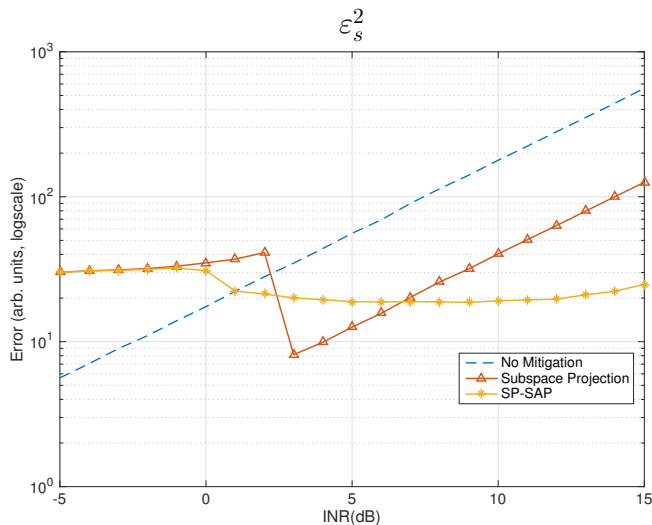


Figure 8. Post-mitigation mean square error in the visibility matrix. Both subspace projection and SP-SAP perform well for low INRs. However, the error in subspace projection begins to diverge at a low INR while SP-SAP achieves lower, stable residuals for a larger range of INRs.

Figure 8 presents the results of the mean squared error determined by (26). This metric is relevant for synthetic imaging because in the absence of RFI and noise \mathbf{R}_s represents the true visibility matrix. Therefore, the mean square error measures how close the filtered signal covariance matrix is to the desired visibility matrix. Over the simulated range of INRs, SP-SAP achieves approximately the same residual level. Subspace projection applied directly across the entire array does slightly out-perform SP-SAP for a small range of INR values. However, there quickly comes a point where as INR increases, so do the residuals, implying that subspace projection is no longer effective. The point at which the residuals for SP-SAP begin to increase is beyond practical INR levels. At that stage, other issues such as non-linearity of the LNAs or saturation in the ADCs become more relevant. Thus we may claim that SP-SAP delivers effective RFI cancellation over a wider INR range than conventional subspace projection.

Figure 9 shows a comprehensive simulated imaging example comparing the two algorithms, and illustrates the success of SP-SAP at better recovering the desired image. The simulation shows a 12-hour observation with 30-minute updates and is the same imaging scenario and array geometry as previously described with an INR of 10 dB. The image formation process is a brute-force approach using a direct computation of the inverse 2-D Fourier transform to recover the intensity values $I(\rho)$ in (4). There is therefore no u - v cell averaging or re-binning to interpolate visibilities onto a rectangular grid, nor is deconvolution used to remove the effects of the dirty beam.

Figure 9(a) shows the original true image phantom used to compute the visibilities along all array baselines. The modeled angular field of view extent for the image was kept very small to push the resolution limits of the array’s dirty beam. As a comparable example of the best achievable result with this array – source geometry and source image scale, (b) shows the computed image with no RFI or noise. Sub-figure (c) shows the resulting image with both noise and RFI present. Using projection-based RFI mitigation the goal is to remove the interferer artifacts seen in (c) to produce an image similar to (b). Applying \mathbf{P}_{SP} and \mathbf{P}_{SAP} to the signal-plus-noise-plus RFI covariance matrix results in Figures 9(d) and (e) respectively. Figure (d) shows that conventional subspace projection removes some interference since faint characteristics of the desired image are beginning to appear. However, SP-SAP results in (e) and more fully recovers the image with no apparent evidence of RFI artifacts or corruption to the desired signal. It is a close match to (b).

The mean squared reconstructed image error, with respect to signal-only Figure 9(b), was computed for the RFI-plus-noise imaging cases. When no RFI canceling was used as in image (c), mean squared error per pixel was $\epsilon_{(c)}^2 = 190.9$. With the conventional subspace projection of image (d), $\epsilon_{(d)}^2 = 64.5$. With the proposed SP-SAP algorithm, error in image (e) dropped dramatically to $\epsilon_{(e)}^2 = 0.372$.

7. CONCLUSIONS

In the growing presence of RFI, sensitive synthesis array instruments will need to rely on methods other than flagging. The simulations presented above show that SP-SAP on large synthesis arrays can improve RFI mitigation on the order of 9 dB as compared to conventional subspace projection across the entire array. Future work could show that other array-based spatial filtering algorithms such as oblique projection (Behrens & Scharf 1994; Hellboug et al. 2012) and cross subspace projection (CSP) (Jeffs et al. 2005) can benefit from subarray processing. For example, in CSP, auxiliary antennas improve INR levels and help achieve better RFI mitigation because there is a more accurate representation of the interference parameters (Jeffs et al. 2005; Sardarabadi et al. 2016). CSP can then benefit by using subarray processing and designating one of the array elements in a subarray as the auxiliary to improve RFI cancellation.

Assumptions made in this work, such as known arrival angles for interferers and correlator dump abilities for STIs are not unrealistic. The interference arrival angle θ_i is only used to determine the propagation vector that determines the effective phase propagation ψ_m for subarray formation. For any satellite or fixed ground-based signal, the arrival angle θ_i is known to high accuracy. Even modest errors in θ_i still yield effective cancellation. Unless the angle of arrival for the interferer is geostationary θ_i will need to be updated reg-

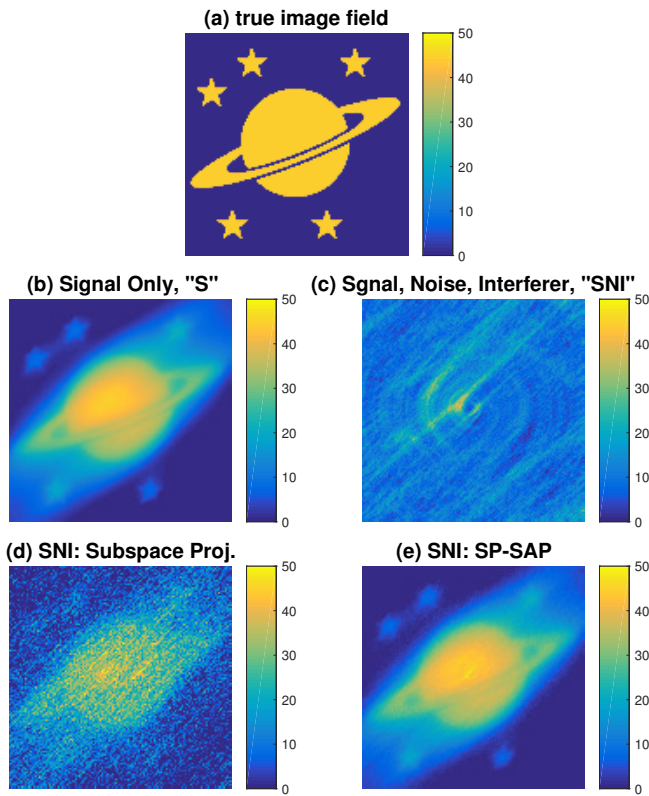


Figure 9. Synthetic imaging simulation comparing subspace projection and SP-SAP. (a) Original image phantom used to generate the observed visibilities (covariance matrices). (b) Image reconstruction with no noise or RFI. Artifacts are due only to the “dirty beam” response of the array sample pattern in the (u, v) plane. (c) Reconstruction in the presence of noise and a strong interferer with INR of 10 dB. (d) Filtered image after applying conventional subspace projection to the entire array. (e) Filtered image after applying SP-SAP to sub arrays. Interference is still very prominent in (d) as only faint characteristics of the SOI are visible. SP-SAP better recovers the image in the presence of RFI.

ularly for each STI along with the calculation of subarray partitions. In the past decade, hardware for correlator designs have advanced such that many observatories can now support dump intervals on ms time scales. This is valuable to mitigate the effect of interferer motion. A correlator which can support rapid integration dumps is already operational in the VLA receiver. We recommend that a comparable system be considered in the design of the ngVLA so that spatial interference mitigation techniques such as SP-SAP can be utilized. Projection-based RFI mitigation algorithms rely on an eigenvalue decomposition, therefore, in the design of the correlator, it is also important that the antenna self-power terms, or the diagonal entries of \mathbf{R}_j be saved out by the correlator.

Spatial filtering techniques such as SP-SAP can be performed offline as part of post-correlation image forming processes. As has been shown, subspace projection techniques can introduce a bias as part of the estimation process, however, that can be corrected for with known bias correction methods (Leshem et al. 2000; Leshem & van der Veen 2000; Raza et al. 2002; Jeffs et al. 2005). There is no risk of data corruption with post-correlation processes because projections can be applied after raw visibilities have been saved.

ACKNOWLEDGEMENTS

This work was funded by the National Science Foundation award AST-1519126 with support from the National Radio Astronomy Observatory as part of the technical community studies program for developing the ngVLA.

REFERENCES

- Anonymous. 2013, Techniques for mitigation of radio frequency interference in radio astronomy, Tech. Rep. ITU-R RA.2126, International Telecommunications Union (ITU), <https://www.itu.int/pub/R-REP-RA.2126-1-2013>
- Behrens, R. T., & Scharf, L. L. 1994, *IEEE Transactions on Signal Processing*, 42, 1413
- Black, R. A. 2017, PhD thesis, Brigham Young University
- Black, R. A., Jeffs, B. D., Warnick, K. F., Hellbourg, G., & Chippendale, A. 2015, in *2015 IEEE Signal Processing and Signal Processing Education Workshop (SP/SPE)*, 261
- Carilli, C. L. 2015, Next Generation Very Large Array Memo Series, 1
- . 2016, Next Generation Very Large Array Memo Series, 1
- Davidson, D. B. 2012, in *ISAPE2012*, 1279
- Ellingson, S. W., Bunton, J. D., & Bell, J. F. 2000, in *Proc. SPIE*, Vol. 4015, 400
- Ellingson, S. W., Bunton, J. D., & Bell, J. F. 2001, *The Astrophysical Journal Supplement Series*, 135, 87
- Ellingson, S. W., & Hampson, G. A. 2002, *IEEE Transactions on Antennas and Propagation*, 50, 25
- Ford, J. M., & Buch, K. D. 2014, in *2014 IEEE Geoscience and Remote Sensing Symposium*, 231
- Fridman, P. A., & Baan, W. A. 2001, *Astronomy and Astrophysics*, 378, 327
- Hellbourg, G. 2015, in *2015 IEEE Signal Processing and Signal Processing Education Workshop (SP/SPE)*, 278
- Hellbourg, G., Weber, R., Capdessus, C., & Boonstra, A. J. 2012, in *2012 IEEE Statistical Signal Processing Workshop (SSP)*, 93

- Hoppmann, L., Staveley-Smith, L., Freudling, W., et al. 2015, *Monthly Notices of the Royal Astronomical Society*, 452, 3726
- Indermuehle, B. T., Harvey-Smith, L., Wilson, C., & Chow, K. 2016, in *2016 Radio Frequency Interference (RFI)*, 43
- Jeffs, B., Warnick, K., Landon, J., et al. 2008, *IEEE Journal of Selected Topics in Signal Processing*, 2, 635
- Jeffs, B. D., Li, L., & Warnick, K. F. 2005, *IEEE Transactions on Signal Processing*, 53, 439
- Jeffs, B. D., Warnick, K., & Li, L. 2003, in *Acoustics, Speech, and Signal Processing, 2003. Proceedings. (ICASSP '03). 2003 IEEE International Conference on*, Vol. 5, V
- Kaveh, M., & Barabell, A. 1986, *IEEE Transactions on Acoustics, Speech, and Signal Processing*, 34, 331
- Kot, A. C., Lee, Y. D., & Babri, H. 1995, *IEE Proceedings - Vision, Image and Signal Processing*, 142, 247
- Landon, J., Jeffs, B. D., & Warnick, K. F. 2012, *IEEE Transactions on Signal Processing*, 60, 1215
- Leshem, A., & van der Veen, A.-J. 2000, *IEEE Transactions on Information Theory*, 46, 1730
- Leshem, A., van der Veen, A.-J., & Boonstra, A.-J. 2000, *Astrophysical Journal Supplements*, 131, 355
- Offringa, A. R., de Bruyn, A. G., Zaroubi, S., et al. 2012, *Astronomy and Astrophysics*, 549, A11
- Otto, A. J., Millenaar, R. P., & van der Merwe, P. S. 2016, in *2016 Radio Frequency Interference (RFI)*, 81
- Raza, J., Boonstra, A. J., & van der Veen, A. J. 2002, *IEEE Signal Processing Letters*, 9, 64
- Sardarabadi, A. M., van der Veen, A. J., & Boonstra, A. J. 2016, *IEEE Transactions on Signal Processing*, 64, 432
- Sokolowski, M., Wayth, R. B., & Lewis, M. 2015, in *2015 IEEE Global Electromagnetic Compatibility Conference (GEMCCON)*, 1
- Swindlehurst, A., Jeffs, B., Seco-Grenados, G., & Li, J. 2013, in *Academic Press Library in Signal Processing*, 1st Edition., ed. R. Chellappa & S. Theodoridis (Academic Press)
- Taylor, G. B., Carilli, C. L., & Perley, R. A., eds. 1999, *Synthesis imaging in radio astronomy II* (Astronomical Society of the Pacific, San Francisco, Calif.)
- Thompson, A. 1982, *IEEE Transactions on Antennas and Propagation*, 30, 450
- Thompson, A., Moran, J., & Jr., G. S. 2001, *Interferometry and synthesis in radio astronomy*, 2nd edn. (Wiley, New York)
- van der Veen, A. J., Leshem, A., & Boonstra, A. J. 2005, in *The Square Kilometre Array: An Engineering Perspective*, ed. P. Hall (Springer Netherlands, Dordrecht), 231
- Vine, D. M. L., Johnson, J. T., & Piepmeier, J. 2016, in *2016 Radio Frequency Interference (RFI)*, 49